UNIVERSIDAD INDUSTRIAL DE SANTANDER

MASTER'S THESIS

A deep learning-based methodology of 2D seismic acquisition geometry design guided by full waveform inversion

Author:
Ana Gabriela Mantilla Dulcey

Advisor:
PhD Henry Arguello Fuentes

A thesis in fulfillment of the requirements
for the degree of Master of Science in Geophysics
presented to Graduate Committee

High Dimensional Signal Processing Group
School of Systems and Computer Engineering
Faculty of Physicomechanical Engineering

April 24, 2026

Metodología basada en aprendizaje profundo para el diseño de geometrías de adquisición sísmica 2D guiada por la inversión de onda completa

Resumen

El objetivo principal del diseño de geometrías de adquisición sísmica es iluminar el subsuelo para identificar posibles reservorios de energía. Los métodos tradicionales de diseño de adquisición incluyen patrones uniformes, aleatorios y jittered. Los patrones uniformes pueden resultar poco prácticos debido a limitaciones físicas, mientras que los patrones irregulares pueden introducir ruido incoherente en los datos por *aliasing*. Los métodos basados en aprendizaje profundo se han enfocado en enfoques basados en datos, regularizados mediante la reconstrucción de la calidad de la señal sísmica, con el fin de diseñar patrones submuestreados. Sin embargo, con frecuencia no se considera el desempeño de la iluminación del subsuelo, especialmente en ambientes de alta complejidad geológica. En este trabajo se introduce ISPO (*Imaging-guided Seismic Pattern Optimization*, por sus siglas en inglés), un enfoque novedoso basado en aprendizaje profundo. ISPO requiere un modelo de velocidades de referencia, a partir del cual un operador de modelamiento directo genera registros de disparos sísmicos. Posteriormente, un modelo probabilístico de difusión basado en aprendizaje profundo produce perturbaciones del modelo de velocidades que son estructuralmente diversas pero geológicamente consistentes. Estas perturbaciones se emplean para entrenar un operador de iluminación o *imaging* que mapea los registros de disparos a modelos de velocidad. El objetivo es optimizar las posiciones de receptores y/o fuentes mediante una capa binaria, guiada por la calidad de reconstrucción de los modelos de velocidad obtenidos a partir del patrón optimizado, permitiendo al mismo tiempo el submuestreo. ISPO fue evaluado en tres escenarios de adquisición: únicamente receptores, únicamente fuentes y submuestreo simultáneo. De manera consistente, ISPO supera tanto a las metodologías clásicas como a las basadas en aprendizaje profundo, incluidas las de diseño uniforme, jittered, aleatorio y las basadas o guiadas por la reconstrucción de datos sísmicos. El método muestra un desempeño superior en métricas de SSIM, MSE y perceptuales, preservando al mismo tiempo las estructuras geológicas.

Objetivos

Objetivo general

Desarrollar una metodología basada en aprendizaje profundo para el diseño de geometrías de adquisición sísmica 2D, guiada por modelos de velocidad de onda P obtenidos a partir de la inversión de onda completa.

Objetivos específicos

1) Crear una base de datos sísmica que integre modelos de velocidad de onda P con sus correspondientes registros de disparos (shot gathers).
2) Implementar un operador basado en aprendizaje profundo que realice la inversión de onda completa para obtener modelos de velocidad de onda P.
3) Desarrollar una metodología de aprendizaje profundo para el diseño de geometrías de adquisición sísmica 2D, fundamentada en el operador de aprendizaje profundo y guiada por modelos de velocidad de onda P.
4) Validar la metodología de diseño sísmico basada en aprendizaje profundo en escenarios geológicos con diferentes complejidades estructurales y estratigráficas.

Pregunta de investigación

¿Cuál es la metodología de diseño de geometrías de adquisición sísmica 2D que permite obtener la mejor iluminación del subsuelo mediante patrones submuestreados?

Imaging guided pattern optimization for seismic acquisition geometries design with deep learning

Ana Mantilla-Dulcey, Henry Arguello, *Senior Member, IEEE*

***Abstract*—The primary purpose of seismic acquisition geometry design is to illuminate the subsurface to identify potential energy reservoirs. Traditional acquisition design methods include uniform, random, and jittered patterns. Uniform patterns can be impractical due to physical constraints, and irregular patterns can introduce incoherent noise to the data through aliasing. Deep learning methods have focused on data-driven approaches, regularized by seismic signal quality reconstruction, for designing undersampled patterns. However, they frequently overlook imaging performance under geological variability. In this work, we introduce ISPO (Imaging-guided Seismic Pattern Optimization), a novel deep learning-based framework. ISPO requires a reference velocity model, from which a forward operator generates modeled shot gathers. A denoising diffusion probabilistic model then produces structurally diverse yet geologically consistent perturbations to the velocity model. These perturbations are used to train an imaging operator that maps shot gathers to velocity models. The central objective is to optimize receiver and/or source positions using a binary layer, guided by the reconstruction quality of the velocity models obtained from the optimized pattern, while allowing for undersampling. ISPO was evaluated across three acquisition scenarios—receiver-only, source-only, and simultaneous undersampling. ISPO consistently outperforms both classical and DL-based baselines, including uniform, jittered, random, and end-to-end reconstruction-driven designs. The method yields superior performance across SSIM, MSE, and perceptual metrics while preserving key structural features of the velocity model even at low acquisition rates.**

***Index Terms*—2D seismic acquisition design, velocity model imaging, deep learning, diffusion models, seismic data reconstruction.**

I. Introduction

EXPLORATION of energy sources such as critical raw materials, hydrogen, or geothermal reservoirs, and carbon capture and storage has become a central focus for the energy transition [1]–[4]. It requires precise subsurface characterization to minimize exploratory risks and support informed decision-making. Seismic reflection remains the most effective geophysical method for imaging complex subsurface structures and identifying potential energy reservoirs [5]–[9]. However, designing an optimal seismic acquisition geometry that ensures effective subsurface illumination remains a significant challenge in geophysical exploration [10]–[17]. This illumination depends on strategically placing seismic sources and receivers, maximizing energy interaction with target reflectors, and optimizing data recording [10].

Existing approaches are categorized into two main types: regular and irregular patterns. Regular patterns used the classical approach, which relies on geological modeling and numerical simulations of seismic wavefields using specialized software such as NORSAR, OMNI, and Nucleus [12], [18]. The uniform pattern is evaluated using geophysical imaging methods, including reverse time migration, velocity model building with full waveform inversion (FWI), Marchenko imaging [19], full wavefield migration [13], and focal beam analysis [15]. While these approaches can ensure regular acquisition patterns and coverage, practical constraints, such as social, economic, or environmental factors, may hinder their application, because seismic sources and receivers are often sparsely distributed.

Irregular patterns introduce variability in receiver locations to account for practical constraints and reduce data acquisition costs. The irregular seismic acquisition design approach includes random, jittered, and optimized patterns. Random and jittered focus on reducing structured aliasing by converting it into incoherent noise, which is suppressed but requires high-quality reconstruction due to undersampling [19]. Optimized patterns seek to balance signal or image quality and acquisition cost by undersampling through optimal experimental design (OED) [20], iterative [21], and deep learning (DL) [22] methods. The OED approach enhances seismic and geophysical data acquisition by maximizing information while minimizing costs and environmental impact [17], [20]. Unlike standard methods, OED adapts to subsurface complexity, improving imaging and inversion results for regular and irregular survey designs. Its key advantage lies in integrating subsurface information to ensure high-quality imaging. [20] outlined a step-by-step optimization process based on eigenvalue analysis, which is computationally demanding. To address this, [17] proposed a sequential receiver-wise optimization strategy for source location, significantly reducing computational costs. Their study focused on FWI and assumed a predefined subsurface model. Notably, they highlighted the potential of reducing the number of sources or receivers in seismic acquisition design without compromising imaging quality.

Iterative methodologies refine seismic acquisition patterns using imaging techniques and compressive sensing. For instance, [14] applied particle swarm optimization to determine receiver location and enhance subsurface coverage. However, irregular receiver configurations can degrade data quality

This work was supported by the Vicerrectoría de Investigación y Extensión of Universidad Industrial de Santander, under Project 4619; and also by the Agencia Nacional de Hidrocarburos and the Ministerio de Ciencia, Tecnología e Innovación under Project 110431 and CTO-045-2025

Ana Mantilla-Dulcey is with the Department of Physics, Universidad Industrial de Santander, Bucaramanga 680002, Colombia (e-mail: ana.mantilla@correo.uis.edu.co)

Henry Arguello is with the Department of Systems Engineering, Universidad Industrial de Santander, Bucaramanga 680002, Colombia (e-mail: henarfu@uis.edu.co)

in shallow anomalies. [19] proposed a compressive-sensing-based survey with sparse, random sampling for Marchenko imaging, using the FISTA algorithm to reconstruct missing seismic data. Similarly, [21] imposed a maximum gap between adjacent sources or receivers and employed a spectral gradient-projection method for data recovery. [16] introduced ergodic sampling to reduce redundancy while maintaining Nyquist-equivalent information, lowering acquisition costs. Other works have proposed a target-oriented strategy based on full-wavefield migration [13], optimizing receiver density per unit area to improve imaging. [15] designed an automated approach to optimize irregular source or receiver geometries, validating results through focal beam analysis and gradient descent. These methodologies integrate imaging constraints to enhance seismic acquisition design. However, their effectiveness depends on the assumptions made about seismic noise and the accuracy of prior knowledge regarding the target depth and extent.

Most DL designs target signal reconstruction rather than imaging fidelity under geological variability [22]–[24]. For instance, [24] combined a convolutional neural network with a genetic algorithm to optimize source and receiver location, outperforming randomized acquisition designs. [22] introduced an end-to-end optimization framework that models the seismic pattern as a deep binary layer, learning optimal source and receiver locations for undersampled acquisition while preserving data quality reconstruction. [25] developed Seis-PDDN, integrating edge-preserving undersampling with diffusion null-space iteration to optimize survey design and data reconstruction. In both cases, the acquisition pattern is evaluated based on the quality of the reconstructed seismic signal. While iterative, classical, and OED methods concentrate on imaging tasks, DL-based methods prioritize reconstruction. However, an effective seismic acquisition geometry design must integrate both aspects to ensure high-quality data recording.

This work proposes ISPO, a DL-based method that unifies imaging and undersampling design in a single optimization framework. ISPO incorporates three tasks for the pattern design: The first task involves acoustic modeling on a reference theoretical velocity model that best describes the geological complexity of the area where the seismic acquisition will be conducted. The second task focuses on undersampling the modeled shot gathers using a trainable binary layer that controls the locations of the acquired receivers or sources. The third task involves imaging by reconstructing velocity models from the modeled and subsampled shot gathers. The ground-truth subsurface model is unknown, and the theoretical velocity model inherently introduces some uncertainty. A practical strategy to ensure the adaptability of the optimized pattern is to test it against a set of realistic velocity-model perturbations that a diffusion model can obtain.

ISPO addresses the trade-off between acquisition cost and subsurface imaging quality by proposing the ISPO method. Our contributions are as follows:

- Imaging-guided design: ISPO is the first DL framework to optimize seismic patterns directly under imaging constraints, rather than solely for signal reconstruction.
- Integration of diffusion-based geological variability: The method incorporates a denoising diffusion probabilistic model to generate geologically plausible perturbations to the reference velocity model, thereby improving the robustness of the learned acquisition patterns to subsurface variability.
- Simultaneous optimization of sources and receivers: ISPO supports flexible design under multiple acquisition scenarios—receiver-only, source-only, and simultaneous undersampling—while preserving structural fidelity in the resulting velocity maps.
- Superior imaging performance: ISPO consistently outperforms classical (uniform, random, jittered) and deep learning-based baselines (including end-to-end reconstruction methods), particularly in SSIM, LPIPS, and MAE under different undersampling rates.

II. Proposed methodology for designing 2D seismic acquisition geometries using deep learning, guided by P-wave velocity models derived from full waveform inversion

The proposed method is illustrated in Fig. 1. It aims to optimize the spatial distribution of sources and receivers while undersampling. As the primary goal of seismic surveys is to enhance illumination of subsurface targets, the approach prioritizes patterns that maximize the accuracy of the reconstructed velocity model. The process begins with a target model representing the geological structure of the area under study. Synthetic shot gathers are computed using acoustic wave simulation in a dense, uniform acquisition setting. The data is then passed through an undersampling operator that defines both the receiver positions and the undersampling ratio. Both dense and undersampled shot gathers are subsequently input into a neural imaging operator trained to recover velocity models. This network is guided by perturbed versions of the reference model, allowing it to infer consistent reconstructions from both complete and sparse measurements.

A. Conditional random generation of perturbed velocity models

This stage involves generating perturbed versions of the reference velocity model for imaging. Let $\mathbf{V} \in \mathbb{R}^{P\times Q}$, be a target velocity model, where P and Q are the number of samples in distance and depth, respectively. The perturbations of $\mathbf{V}$ are denoted as $\mathbf{V}^* \in \mathbb{R}^{P\times Q}$ and were generated by training a denoising diffusion probabilistic model (DDPM) [26], [27] as illustrated in 1.

1) Theory and training of the DDPM: A Denoising Diffusion Probabilistic Model (DDPM) is a generative model that learns to create realistic data (such as images or physical fields) by gradually removing noise from random signals. The central idea is simple: if we know how to progressively destroy a signal by adding noise, we can train a neural network to reverse this process and reconstruct meaningful structure from noise. DDPMs were introduced as a principled probabilistic framework for generation, based on a forward diffusion process and a learned reverse denoising process.

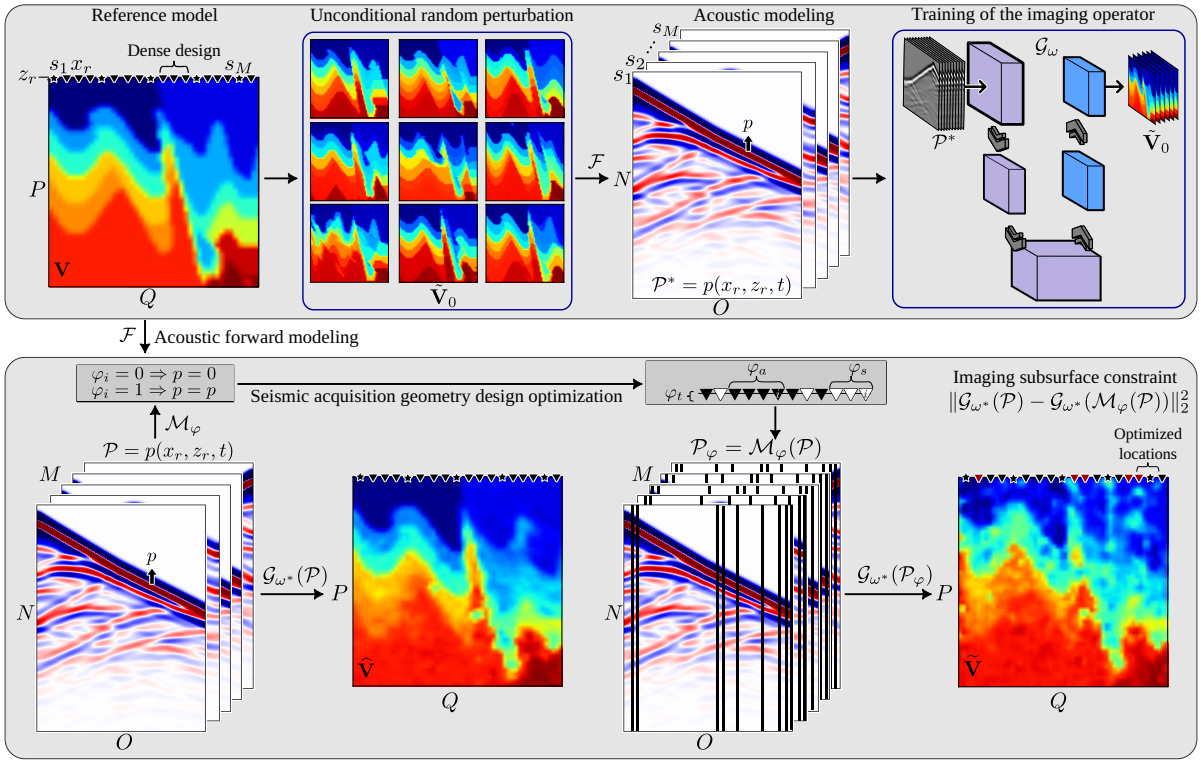

Fig. 1. Proposed method. First, a forward operator $\mathcal{F}$ generates shot gathers $\mathcal{P}$ from a reference velocity model $\mathbf{V}$. Second, a trainable binary layer $\mathcal{M}_\varphi$ subsamples $\mathcal{P}$, producing $\mathcal{P}_\varphi$. Third, an imaging operator $\mathcal{G}_\omega$ calculates $\widetilde{\mathbf{V}}$ and $\widehat{\mathbf{V}}$, corresponding to the velocity model obtained from the optimized and dense pattern, respectively. The process iterates until $\widetilde{\mathbf{V}}$ and $\widehat{\mathbf{V}}$ are consistent in geological structure and velocity values.

Forward diffusion process (adding noise)

The forward process is a fixed, known procedure that gradually corrupts a clean sample (x_0) by adding small amounts of Gaussian noise over many steps. After many steps, the signal becomes almost pure noise. At each step $(t = 1, \ldots, T)$, a small amount of random noise is added:

- Early steps: the data is only slightly corrupted.
- Later steps: the data becomes increasingly noisy.
- Final step: the sample resembles random Gaussian noise.

This process is designed to directly generate a noisy version (x_t) of the original data at any step (t).

Reverse denoising process (learning to remove noise)

The goal of training is to learn the reverse process: starting from noise and gradually recovering structure. A neural network is trained to predict the noise that was added at each step. Given a noisy input (x_t) and the step index (t), the network estimates the noise component and subtracts it. By repeating this denoising operation step by step, the model transforms pure noise into a realistic sample. This procedure can be interpreted as teaching the model to perform many small denoising tasks rather than one large reconstruction. Each task is simple, but their composition produces a complex structure.

Training algorithm (simplified)

- Sample a clean data point (x_0) from the dataset.
- Sample a random time step $(t \in \{1, \ldots, T\})$.
- Sample Gaussian noise (ε).
- Create a noisy sample (x_t) by adding noise to (x_0).
- Use the neural network to predict the noise from $((x_t, t))$.
- Update the network parameters by minimizing the squared error between true and predicted noise.
- Repeat until convergence.

Sampling (generation) algorithm

- Start from random Gaussian noise (x_T).
- For $(t = T, \ldots, 1)$:
  quad Predict the noise in (x_t) using the network.
  quad Remove part of the noise to obtain (x_{t-1}).
  quad Add a small amount of controlled randomness.
- Output (x_0) as the generated sample.

To limit the random generation to plausible solutions of the target velocity model, the sampling process is computed in Algorithm 2. Here k is the velocity conditional time step, $\alpha_t = 1 - \beta_t$, with β_t as the scheduler, $\tilde{\alpha}_t = \prod_{s=0}^{t} \alpha_s$, and ϵ_ς is the diffusion model with trainable parameters ς.

The selection of the velocity conditional time step k depends on each velocity model; if k is big, the resulting models will be strongly different from the target model, and if k is small, the models will be similar in structure and velocity values, as shown in Fig. 2. This strategy allows the training domain to be limited, establishing a range of plausible solutions for subsurface imaging.

These perturbations preserve the main geological structure while introducing realistic deviations, thus enhancing the model's robustness to potential discrepancies in real-world scenarios. The perturbed velocity models differ from the target model in layer thickness changes, layer count, geometric variations, and discontinuities. In real-world scenarios, the ground-truth subsurface model is unknown, and traditional

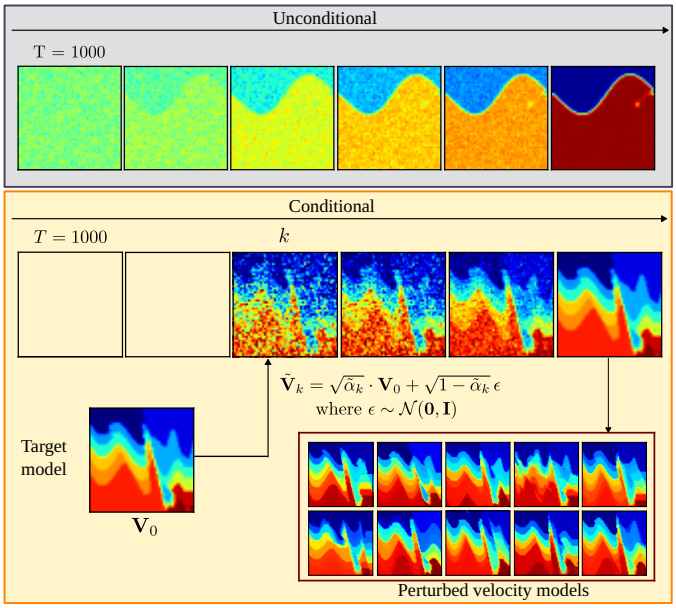

Fig. 2. (Upper) Unconditional random generation and (bottom) conditional diffusion synthesis of perturbations using a target velocity model from a diffusion step k.

methods for seismic acquisition geometry design estimate a reference theoretical velocity model given historical geophysical surveys, well logs, and geological information [12], [18].

Algorithm 1 Training process

Require: T ▷ Total number of diffusion steps

1: **repeat**
2: $\mathbf{V}_0 \sim q(\mathbf{V}_0)$ ▷ Sample a velocity model
3: $t \sim \text{Uniform}(\{1, \ldots, T\})$
4: $\boldsymbol{\epsilon} \sim \mathcal{N}(\mathbf{0}, \mathbf{I})$
5: Take a gradient descent step on:

$$\nabla_\theta \left\| \boldsymbol{\epsilon} - \boldsymbol{\epsilon}_\varsigma\left(\sqrt{\tilde{\alpha}_t}\,\mathbf{V}_0 + \sqrt{1-\tilde{\alpha}_t}\,\boldsymbol{\epsilon},\ t\right)\right\|^2$$

6: **until** convergence

Algorithm 2 Velocity conditional sampling process

Require: $k, \mathbf{V}_0$ ▷ Velocity conditional time step and target velocity model

1: $\epsilon \sim \mathcal{N}(\mathbf{0}, \mathbf{I})$
2: $\tilde{\mathbf{V}}_k = \sqrt{\tilde{\alpha_k}}\mathbf{V}_0 + \sqrt{1-\tilde{\alpha_k}}\epsilon$
3: **for** $t = k, ..., 1$ **do**
4: $\mathbf{z} \sim \mathcal{N}(\mathbf{0}, \mathbf{I})$ if $t > 1$, else $\mathbf{z} = \mathbf{0}$
5: $\tilde{\mathbf{V}}_{t-1} = \frac{1}{\sqrt{\alpha_t}}\left(\tilde{\mathbf{V}}_t - \frac{1-\alpha_t}{\sqrt{1-\tilde{\alpha}_t}}\epsilon_\varsigma(\tilde{\mathbf{V}}_t, t)\right) + \sqrt{1-\alpha_t}\mathbf{z}$
6: **end for**
7: **Return** $\tilde{\mathbf{V}}_0$ ▷ Perturbed velocity models

B. Acoustic forward modeling

The modeling process involves computing the seismic wavefield in the reference velocity model to generate synthetic shot gathers. A forward modeling operator $\mathcal{F}$ simulates the propagation of the wavefront. The following expression is based on the acoustic wave equation of an isotropic medium.

$$\frac{1}{v^2(x,z)}\frac{\partial^2 p}{\partial t^2} - \nabla^2 p = S(x,t), \tag{1}$$

where v is the velocity value in $\mathbf{V}$, p is the pressure wavefield, t denotes time, x and z are the distance and depth, respectively, and $S(s_x, s_z, t)$ is the seismic source. The amplitude $A(t)$ of the seismic source is represented by a Ricker wavelet [28] with a peak frequency f and is given by:

$$A(t) = (1 - 2\pi^2 f^2 t^2)e^{-\pi^2 f^2 t^2}, \tag{2}$$

$$S(x,z,t) = A(t)\delta(x - s_x)\delta(z - s_z), \tag{3}$$

where s_x and s_z represent the coordinate position of the source (or shot). Let $\mathbf{s}_x \in \mathbb{N}$ and $\mathbf{s}_z \in \mathbb{N}$ be the vectors representing the positions of all seismic shots in the x and z-axis, respectively. The numerical solution was computed using a second-order finite-difference scheme in time and eighth-order in space. The discretized wave equation in Appendix A represents the finite-difference formulation of the acoustic wave propagation.

Suppose we have a set of receivers with positions $(\mathbf{r}_x, \mathbf{r}_z)$, where $\mathbf{r} \in \mathbb{R}$. The seismic record in a receiver is given by $p(x = r_x, z = r_z, t)$, which can be represented as p_O, where O is the number of receivers. The pressure wavefield in a receiver O and time index n is given by $p_O^n = p_{r_x, r_z}^n$. The value of p for all n in a receiver O is stored as $p_O^n = \{p_O^0, p_O^1, p_O^2, \ldots, p_O^n\}$, which represents a seismic trace or column. The p_O values form a seismic shot as $\mathcal{P} = \{p_1, p_2, p_3, ..., p_O\}$. The output of the wavefront propagation is a set of synthetic seismic shot gathers $\mathcal{P} \in \mathbb{R}^{M \times N \times O}$, where M is the number of shots, N the time samples, and O the receivers.

$$\mathcal{P} = \mathcal{F}(\mathbf{V}, \mathbf{r}_x, \mathbf{r}_z, \mathbf{s}_x, \mathbf{s}_z, \lambda, \Delta x, \Delta z, \Delta t, f, t). \tag{4}$$

C. Seismic subsampling pattern optimization

This task aims to determine the receiver locations that should be removed, given a desired acquired rate. The output of the undersampling process is called $\mathcal{P}_\varphi \in \mathbb{R}^{M \times N \times O}$. A single shot can be modeled as:

$$\mathcal{P}_\varphi^i = \boldsymbol{\Phi} \odot \mathcal{P}^i, \quad i = 1, 2, \ldots, M, \tag{5}$$

where i indexes the number of shots, which means $\mathcal{P}_\varphi^i \in \mathbb{R}^{N \times O}$, $\odot$ is the Hadamard product, $\boldsymbol{\Phi} \in \{0,1\}^{N \times O}$ is the subsampling operator that sets to zero the positions of removed receivers or shots [23]. The subsampling operator changes according to receivers, sources, or both, pattern, as described as follows:

1) Receivers pattern design: The receivers are represented by the columns of each $\mathcal{P}^i$, and the mask $\boldsymbol{\Phi}_R$ is invariant, meaning that all shots have the exact positions of acquired and removed receivers. The following equation models the process:

$$\boldsymbol{\Phi}_R = \mathbb{1}_N \otimes \mathbf{s}_R, \quad \text{where } \mathbf{s}_R \in \{0,1\}^{1 \times O}. \tag{6}$$

The vector $\mathbf{s}$ represents the positions of acquired and removed receivers, denoted as one and zero, respectively. $\otimes$ denotes the Kronecker product, and $\mathbb{1}_N$ is an N-dimensional one-valued vector.

2) Shots pattern design: The shots are represented by all the columns of the input data, which means that if a single shot is removed, $\mathcal{P}^i = 0$. In this case, the mask $\mathbf{\Phi}_P$ varies across the M positions. The process is described as follows:

$$\mathbf{\Phi}_P = \begin{cases} \mathbf{0}_N \otimes \mathbf{s}_P & \text{if } M \in L, \\ \mathbb{1}_N \otimes \mathbf{s}_P & \text{otherwise}, \end{cases} \tag{7}$$

where L represents the positions of the removed shots, and $\mathbf{s}_P \in \{0,1\}^{1\times M}$.

3) Simultaneous receivers and shots pattern design: The seismic pattern that removes both receivers and shots is represented by the zeroed columns, or by $\mathcal{P}^i$. The mask called $\mathbf{\Phi}$ is composed of the mask of receivers and shots as follows:

$$\mathbf{\Phi} = \mathbf{\Phi}_R \odot \mathbf{\Phi}_P \tag{8}$$

The primary goal is to find a vector $\mathbf{s_R}$ or $\mathbf{s_P}$ that yields the best reconstruction of the velocity model; therefore, a differentiable modeling approach is required. This work optimizes a real-valued parameter $\varphi \in \mathbb{R}^{N\times O}$ such that:

$$\mathbf{s} = f(\varphi), \tag{9}$$

$$f(\varphi) = \frac{1}{2}(\text{sign}(\varphi) + 1), \tag{10}$$

where $\frac{\partial f(\varphi)}{\partial \varphi} = 0 \quad \text{for } \varphi \neq 0$. This leads to a vanishing-gradient problem, in which backpropagation yields $\frac{\partial \mathcal{L}}{\partial \varphi} = 0$. The straight-through estimator (STE) [29], [30] is applied, approximating the gradient as $\frac{\partial \mathcal{L}}{\partial \varphi} = 1$, enabling real-valued weight updates. A binary differentiable layer $\mathcal{M}_\varphi : \mathbb{R}^{M\times N\times O} \to \mathbb{R}^{M\times N\times O}$ is defined by:

$$\mathcal{M}_\varphi(\mathcal{P}) = [\mathbf{\Phi}_J \odot \mathcal{P}^{(1)}, \mathbf{\Phi}_J \odot \mathcal{P}^{(2)}, ..., \mathbf{\Phi}_J \odot \mathcal{P}^{(M)}]. \tag{11}$$

The layer $\mathcal{M}_\varphi$ is linear in $\mathcal{P}$, and $\mathbf{\Phi}_J$ represents the undersampling case (Equations 6 - 8). The undersampled shots are given by $\mathcal{P}_\varphi = \mathcal{M}_\varphi(\mathcal{P})$. The expression which controls the acquired rate is given by:

$$\mathcal{L}_R = \left(\frac{\|f(\varphi_R)\|_1}{O} - \gamma_R\right)^2, \tag{12}$$

$$\mathcal{L}_P = \left(\frac{\|f(\varphi_P)\|_1}{M} - \gamma_P\right)^2, \tag{13}$$

$$\mathcal{L}_B = \mathcal{L}_R + \mathcal{L}_P, \tag{14}$$

where $\gamma_R = \frac{T}{O}$, $\gamma_P = \frac{T}{M}$ and T is the desired number of acquired receivers or shots. This means γ denotes the target fraction of ones. The terms φ_R and φ_P denote the trainable parameters for the receivers and shots, respectively. Considering Equation 4 and the perturbed velocity models $\tilde{\mathbf{V}}_0$ obtained from Algorithm 2.

The proposed method lies in the fact that if the seismic pattern design is optimal and ensures proper illumination of seismic energy in the subsurface, the velocity model obtained from the optimized design $\widetilde{\mathbf{V}} = \mathcal{G}_{\omega^*}(\mathcal{P}_\varphi)$ will be consistent in velocities and geological structures compared to the model estimated using the dense, uniform design $\widehat{\mathbf{V}} = \mathcal{G}_{\omega^*}(\mathcal{P})$ as follows:

Receivers pattern design

$$\varphi_R^* = \arg\min_{\varphi_R} \frac{\rho_1}{MNO} \|\mathcal{G}_{\omega^*}(\mathcal{M}_{\varphi_R}(\mathcal{P})) - \mathcal{G}_{\omega^*}(\mathcal{P})\|_2^2 + \rho_2 \mathcal{L}_\mathcal{R}, \tag{15}$$

Shots pattern design

$$\varphi_P^* = \arg\min_{\varphi_P} \frac{\rho_1}{MNO} \|\mathcal{G}_{\omega^*}(\mathcal{M}_{\varphi_P}(\mathcal{P})) - \mathcal{G}_{\omega^*}(\mathcal{P})\|_2^2 + \rho_2 \mathcal{L}_P, \tag{16}$$

Simultaneous receivers and shots pattern design

$$\varphi_B^* = \arg\min_{\varphi_B} \frac{\rho_1}{MNO} \|\mathcal{G}_{\omega^*}(\mathcal{M}_{\varphi_B}(\mathcal{P})) - \mathcal{G}_{\omega^*}(\mathcal{P})\|_2^2 + \rho_2 \mathcal{L}_B, \tag{17}$$

where ρ_1 denotes the influence of the velocity model reconstruction, and ρ_2 controls the acquired rate convergence. The trainable parameter $\varphi_B = \{\varphi_R, \varphi_P\}$.

Algorithm 3 ISPO Proposed method

Require: $k, \mathbf{V}, \mathbf{r}_x, \mathbf{r}_z, \mathbf{s}_x, \mathbf{s}_z, \lambda, \Delta x, \Delta z, \Delta t, f, t, \rho_1, \rho_2$

Generate perturbed velocity models $\tilde{\mathbf{V}}_0$ with Algorithm 2
for each s in M **do** ▷ Number of shots
  for l in N **do** ▷ Number of time steps
    $\mathcal{P}^* = \mathcal{F}(\tilde{\mathbf{V}}_0, \mathbf{r}_x, \mathbf{r}_z, \mathbf{s}_x, \mathbf{s}_z, \lambda, \Delta x, \Delta z, \Delta t, f, t)$
    $\mathcal{P} = \mathcal{F}(\mathbf{V}, \mathbf{r}_x, \mathbf{r}_z, \mathbf{s}_x, \mathbf{s}_z, \lambda, \Delta x, \Delta z, \Delta t, f, t)$
  end for
end for
Train the imaging operator using Adam optimizer

$$\omega^* = \arg\min_{\omega} \frac{1}{PQ} \left\|\mathcal{G}_\omega(\mathcal{P}^*) - \tilde{\mathbf{V}}_0\right\|_2^2$$

for $1, ..., E$ **do** ▷ Number of epochs
  $\widehat{\mathbf{V}} = \mathcal{G}_{\omega^*}(\mathcal{P})$ ▷ Velocity map from uniform pattern
  $\widehat{\mathbf{V}} \leftarrow \mathcal{G}_{\omega^*}(\mathcal{P}_\varphi)$ ▷ Velocity map from optimized pattern
  Optimize the seismic pattern with imaging constraints

$$\varphi_c^* = \arg\min_{\varphi_c} \frac{\rho_1}{MNO} \left\|\widehat{\mathbf{V}} - \widetilde{\mathbf{V}}\right\|_2^2 + \rho_2 \mathcal{L}_c, \qquad c \in \{R, P, B\}.$$

end for
Return φ^*

Remark: The proposed method establishes a novel baseline for seismic acquisition design by explicitly optimizing receiver or source patterns to enhance subsurface illumination, similar in objective to classical tools. However, unlike traditional approaches, this deep learning-based framework enables optimization guided by velocity model consistency,

offering greater robustness to geological variability and adaptability to real-world constraints. Furthermore, its differentiable architecture facilitates seamless integration with modern reconstruction-based seismic workflows, making it a scalable and flexible alternative for next-generation survey planning. The motivation for using velocity models lies under three key assumptions. First, these models provide representations of complex geological structures, making them essential for optimizing seismic acquisition design to improve subsurface illumination. Second, state-of-the-art seismic geometry design methods depend on prior subsurface information, primarily velocity models, which are also widely used in processing workflows such as common reflection points, common midpoints, and shot gathers. This allows survey design to be optimized based on geological priors. Third, velocity models can be computed using differentiable deep learning-based operators, enabling seamless integration with other algorithms. A key advantage of this approach is its adaptability, which allows for the incorporation of various constraints, such as seismic inversion, denoising, migration, and attributes, based on data availability. Algorithm 3 summarizes the proposed DL-based method.

III. Numerical simulations

A. Perturbed velocity models

The 2D velocity models were obtained from OpenFWI [31], which includes a set of benchmark datasets with varying geological settings and velocity scenarios. The velocity maps were resized to 128×128 samples in time and space. The training for the DDPM was conducted using all data from the 10 families in the database. The computational setting involves a cosine noise schedule defined by $1 - \alpha$ from 10^{-4} to 0.02, with $T = 1000$ diffusion steps. The diffusion model ϵ_ς was trained for 1000 epochs, batch size of 50, and learning rate of 3×10^{-4}. The sampling process was computed separately for five velocity models from the CurveFault-B family (hereafter referred to as model A-E), each with 100 perturbed versions. The 3D velocity model was created using GemPy [32]. A velocity value was assigned to each geological layer. The model is $\mathbf{V} \in \mathbb{R}^{64\times64\times64}$. The seismic acquisition geometry design for the dense and uniform pattern includes: 1000 ms of total simulation, source Ricker wavelet with frequency of 10 Hz, a 64×64 grid of receivers for x and y-axis, each one spaced 10 m, with a depth of 20 m. The total number of seismic sources was set to 20, equally spaced. This line of sources was in the middle of the velocity grid. This acquisition process corresponds to a swath geometry.

B. Seismic modeling

To compute seismic wavefront propagation, the algorithm developed by [33] with the absorbing boundary condition was rewritten in a differentiable PyTorch framework. The 2D acquisition geometry setting to generate $\mathcal{P}$ and $\mathcal{P}^*$ includes $P = Q = 128$, $\Delta x = \Delta z = 1$ m, $\lambda = 120$ absorbing boundary cells, $t = 1024$ ms of total simulation with a time step $\Delta t = 1 \times 10^{-4}$ s. The Ricker wavelet with a frequency of $f = 12$ Hz was used. The total number of shots was 10 with a separation of 12.8 m, and 128 receivers spaced 1 m each. The final database consisted of $\mathcal{P}^* \in \mathbb{R}^{10\times1024\times128}$, and $\mathcal{P} \in \mathbb{R}^{10\times1024\times128}$. The 3D acquisition geometry corresponds to a swath, whose settings include 1000 ms of total simulation, a source Ricker wavelet with frequency of 10 Hz, a 64×64 grid of receivers for x and y-axis, each one spaced 10 m, with a depth of 20 m. The total number of seismic sources was set to 20, equally spaced. This line of sources was in the middle of the velocity grid.

C. Evaluation metrics

To quantitatively evaluate the quality of the velocity models, we employed the Learned Perceptual Image Patch Similarity (LPIPS) [34], Mean Squared Error (MSE), Mean Absolute Error (MAE), and Structural Similarity Index (SSIM) metrics following [31]. For the reconstructed seismic signal at the receiver's location, we used the Peak Signal to Noise Ratio (PSNR) and Signal to Noise Ratio (SNR) as considered in [22], [23]. The proposed method was compared in terms of velocity model reconstruction with baseline patterns uniform, random, and jittered, as well as with the end-to-end approach presented in [22], which focuses on seismic pattern design based on the quality of seismic shot reconstruction.

D. Implementation of an operator based on deep learning that performs full waveform inversion to obtain P-wave velocity models

Full-waveform inversion (FWI) is an imaging method that uses wavefield information from seismic shot gathers to reconstruct subsurface parameters, such as P-wave velocity [35]. FWI can be addressed by two groups of methods: physics-based and deep learning-based. The first group relies on computationally intensive, highly data-dependent nonlinear optimization techniques [36]. These methods have challenges related to high computational cost, strong dependence on the initial velocity model, parameterization, and objective function [36]. The second group includes data-driven methods [37]–[42]. The main limitation lies in their poor ability to generalize, which depends on the size of the training dataset. Given that seismic acquisition design depends on prior information, which may or may not be based on previous campaigns, and that FWI is computationally intensive, the data-driven approach was selected for the inversion process. This is possible due to recent advances in neural networks for full-waveform inversion, which leverage graphics processing units to reduce computational cost.

The following equation represents the forward process of seismic inversion:

$$\mathbf{d} = \mathcal{F}(\mathbf{m}), \tag{18}$$

where $\mathbf{d}$ are the recorded data, $\mathcal{F}$ the forward modeling, and $\mathbf{m}$ the subsurface property. The inverse process can be expressed as:

$$\mathbf{m} = \mathcal{F}^{-1}(\mathbf{d}), \tag{19}$$

However, the operator $\mathcal{F}^{-1}$ is not explicitly defined because it corresponds to the partial differential wave equation. Therefore, the inverse operator was approximated with a neural network as [9], [31], [35], [37], [40]:

$$\mathcal{F}^{-1} \approx \mathcal{G}_\omega, \tag{20}$$

where $\mathcal{G}_\omega$ represents a neural network with trainable parameters ω which compute the inversion process.

Implementation and training: The main goal is to find the optimum values for ω, which, given some seismic data, compute the corresponding velocity model. Therefore the imaging operator $\mathcal{G}_\omega : \mathbb{R}^{M\times N\times O} \to \mathbb{R}^{P\times Q}$. This is expressed as the following optimization process:

$$\omega^* = \arg\min_{\omega} \frac{1}{PQ} \left\| \mathcal{G}_\omega(\mathcal{P}^*) - \mathbf{V}^* \right\|_2^2, \tag{21}$$

where $\mathcal{P}^* = \mathcal{F}(\tilde{\mathbf{V}}_0)$ are the seismic shots obtained from the acoustic modeling in the perturbed velocity models. In this case, $\mathcal{G}_\omega$ has an Attention u-net architecture [43]. It was trained using a supervised deep learning approach, separately for each perturbed velocity model $\tilde{\mathbf{V}}_0$. The computational setting involved a batch size of 16, Adam optimizer, 1×10^{-4} learning rate, and 500 epochs.

E. Implementation details

The seismic pattern optimization used Adam optimizer, a learning rate of 1×10^{-3}, and 5000 epochs. To ensure the geophysical term has enough importance in the seismic design and that the subsampling rate and loss function converge, ρ_1 and ρ_2 were set as:

1) **Receivers pattern design:** $\rho_1 = 16^{-0.001E}$, where E is the number of epochs, and $\rho_2 = 16$.
2) **Shots pattern design:** $\rho_1 = 16^{-0.0001E}$, and $\rho_2 = 16$.
3) **Simultaneous receivers and shots pattern design:** $\rho_1 = 1$, and $\rho_2 = 1$.

The computations for seismic pattern optimization were performed on a graphics processing unit (GPU), specifically an NVIDIA GeForce RTX 4070 with 12 GB of memory, highlighting the method's computational efficiency.

F. Geological setting of the dataset

Model A, G: exhibits lateral variations in layer thickness and gently folded geometries. In the left-hand sector, folds are observed in association with a reverse fault that disrupts the continuity of the units. Velocity increases progressively with depth, with no evidence of velocity inversion.

Model B: shows a strong structural control, where a fault system produces horst-and-graben configurations, accompanied by a syncline on the right-hand side. In the central region, a high-displacement reverse fault causes a marked discontinuity of the units. Velocity increases consistently with depth, with no indication of inversion.

Model C, F: displays gentle folding in the left sector, with moderate lateral variations in layer thickness. A fault in the central area disrupts the lateral continuity. On the right-hand side, a synclinal fold is identified, producing greater changes in layer thickness. No evidence of inversion is observed.

Model D: exhibits lateral variations in layer thickness. On the right-hand side, a low-velocity intrusive body stands out, interrupting lateral continuity. Towards the center and left, the units show increased deformation, with folds and subtle changes in layer thickness. Although this inversion dominates the right-hand region, the remainder of the model shows no evidence of inversion.

Model E: displays anticline and syncline structures on the left-hand side, where the units maintain good lateral continuity. Toward the center, an almost vertical high-displacement fault is identified. On the right-hand side, the units appear more deformed, with greater variations in layer thickness. Velocity increases consistently with depth, with no evidence of inversion.

G. Experiment I: Receivers pattern design

This experiment evaluates imaging performance across the baseline patterns, E2E, and the proposed method at different acquisition rates for receiver pattern optimization. Table I shows greater degradation in reconstructing and achieves superior performance across all evaluation metrics. These improvements are particularly notable at low acquisition rates, where traditional patterns exhibit increased degradation in the reconstruction of the velocity models. These results demonstrate that optimizing acquisition through inversion-guided learning better preserves geological structures, whereas the other pattern designs tend to introduce spatial artifacts and loss of detail. Qualitative results are shown in models A-C of Fig. 3. The optimized pattern consistently preserves layer continuity and fault boundaries, while baseline methods exhibit spatial artifacts and structural degradation. The optimized reconstructions are visually more accurate, particularly in regions with structural curvature and discontinuities, where the other patterns tend to fail.

H. Experiment II: Shots pattern design

This experiment aims to evaluate the reconstruction of velocity models when seismic sources are missing. Table II shows the reconstructed metrics accuracy. The proposed method consistently outperforms alternative strategies across most settings, particularly in challenging acquired regimes where $\gamma = 40\%$ and $\gamma = 30\%$, demonstrating its robustness and adaptability. While the uniform pattern yields competitive results at higher acquisition rates, it lacks adaptability. It is sensitive to geological complexity, which may lead to suboptimal illumination in real-world applications. In contrast, our method leverages velocity-model-driven learning to optimize shot configurations, yielding more stable and generalizable performance. The apparent advantage of uniformity in isolated metrics does not reflect its practical limitations in complex subsurface scenarios, where learning-based strategies like ours better capture illumination requirements and structural variability. Fig. 3 illustrates the reconstructed velocity models for Model D and Model E. Notably, the uniform and jittered strategies exhibit symmetric or semi-regular source arrangements,

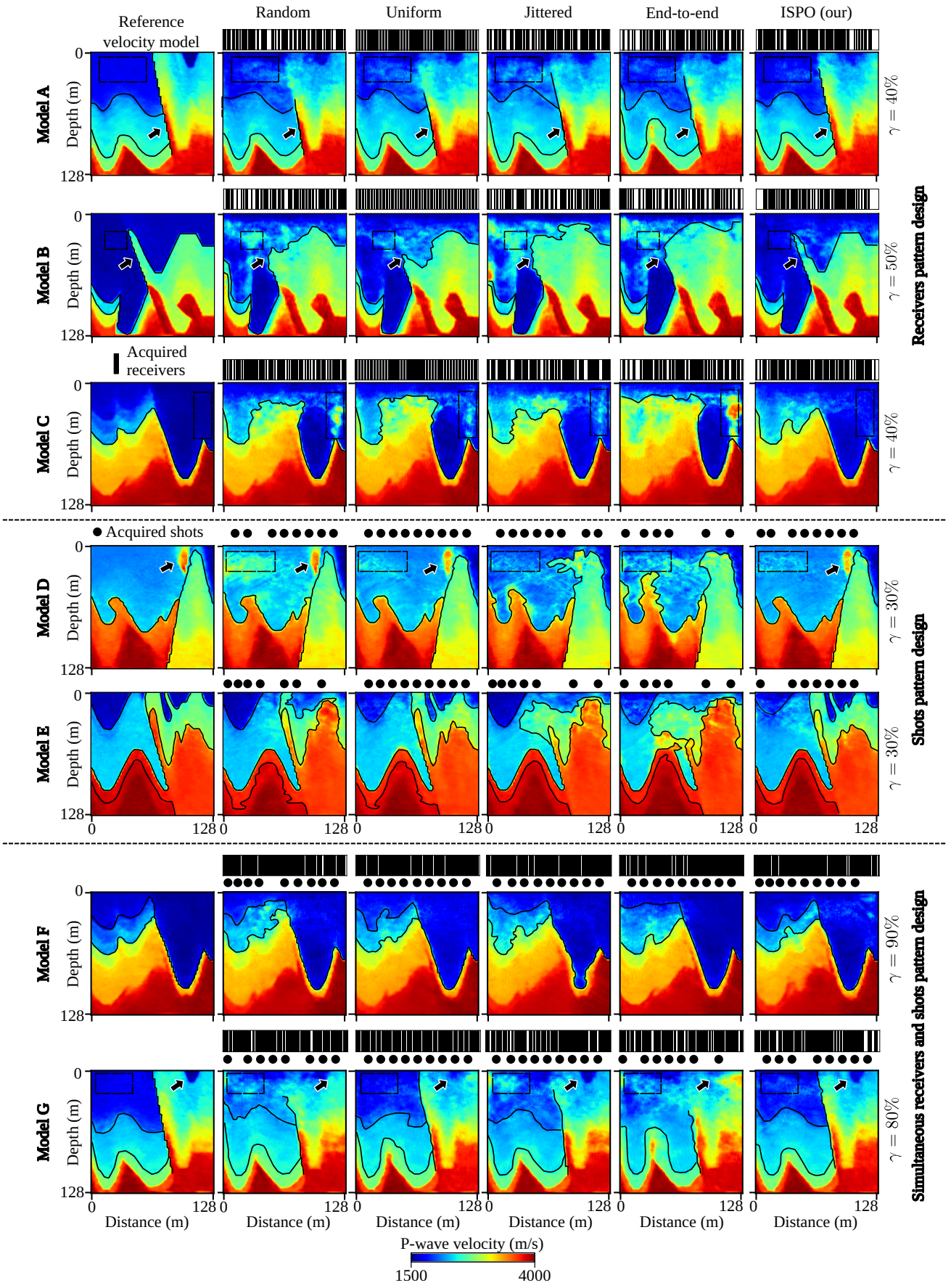

Fig. 3. Comparison of reconstructed velocity models using different acquisition patterns—random, uniform, jittered, and the proposed optimized design—across five structurally distinct test cases (Models A–E). Black lines represent removed receivers, and gray boxes are the removed shots.

TABLE I

RECEIVER PATTERN DESIGN. QUANTITATIVE METRICS COMPARISON FOR THE VELOCITY MODELS A-C AT DIFFERENT UNDERSAMPLING RATES. MSE AND MAE VALUES ARE IN THE ORDER OF $\times 10^{-2}$. BOLD NUMBERS REPRESENT THE BEST PERFORMANCE METRIC.

%γ	Uniform				Jittered				Random				End-to-end				ISPO (our)			
	LPIPS↓	MSE↓	MAE↓	SSIM↑	LPIPS↓	MSE↓	MAE↓	SSIM↑	LPIPS↓	MSE↓	MAE↓	SSIM↑	LPIPS↓	MSE↓	MAE↓	SSIM↑	LPIPS↓	MSE↓	MAE↓	SSIM↑
90	0.056	0.2	3.0	0.883	0.062	0.2	3.1	0.878	0.057	0.2	3.0	0.883	**0.048**	0.200	2.8	0.894	0.048	**0.2**	**2.8**	**0.895**
80	0.107	0.5	4.0	0.820	0.108	0.5	4.7	0.816	0.106	0.6	4.7	0.818	0.108	0.600	4.9	0.817	**0.092**	**0.4**	**4.1**	**0.833**
70	0.175	1.4	7.0	0.742	0.184	1.6	7.6	0.727	0.168	1.5	7.1	0.741	0.178	1.600	7.5	0.733	**0.142**	**0.8**	**5.7**	**0.777**
60	0.240	2.8	10.1	0.658	0.245	3.1	10.7	0.648	0.231	2.8	9.9	0.667	0.259	4.600	12.1	0.630	**0.180**	**1.3**	**7.3**	**0.727**
50	0.280	5.4	13.9	0.576	0.294	5.8	14.6	0.567	0.278	4.7	13.0	0.596	0.318	10.100	18.0	0.528	**0.233**	**2.2**	**9.5**	**0.666**

TABLE II

SHOT PATTERN DESIGN. COMPARISON OF AVERAGE QUANTITATIVE METRICS FOR VELOCITY MODELS D-E AT DIFFERENT UNDERSAMPLING RATES. MSE AND MAE VALUES ARE IN THE ORDER OF $\times 10^{-2}$. BOLD NUMBERS REPRESENT THE BEST PERFORMANCE METRIC.

%γ	Uniform				Jittered				Random				End-to-end				ISPO (our)			
	LPIPS↓	MSE↓	MAE↓	SSIM↑	LPIPS↓	MSE↓	MAE↓	SSIM↑	LPIPS↓	MSE↓	MAE↓	SSIM↑	LPIPS↓	MSE↓	MAE↓	SSIM↑	LPIPS↓	MSE↓	MAE↓	SSIM↑
90	**0.092**	**0.3**	**3.2**	**0.836**	0.112	0.6	3.9	0.799	0.114	0.5	3.8	0.795	**0.139**	0.6	4.2	0.758	0.106	0.5	3.7	0.808
80	**0.076**	0.8	5.2	0.848	0.101	1.4	6.3	0.815	0.108	1.5	6.7	0.812	0.117	1.2	6.8	0.802	0.078	**0.7**	**4.8**	**0.845**
70	0.134	**1.4**	**7.7**	0.772	0.158	4.0	10.5	0.740	0.154	3.3	10.2	0.742	0.257	16.7	23.5	0.570	**0.134**	1.8	**8.0**	**0.774**
60	**0.148**	**1.7**	**8.4**	0.749	0.171	4.5	11.5	0.721	0.170	4.1	11.5	0.721	0.237	15.7	21.8	0.617	0.145	2.0	**8.5**	**0.765**
50	0.215	6.0	14.9	0.661	0.244	12.1	19.2	0.611	0.241	10.2	18.3	0.614	0.336	20.9	28.1	0.444	**0.201**	**4.1**	**12.9**	**0.681**

which often yield coherent reconstructions in simpler regions but tend to introduce velocity artifacts in more complex areas. For instance, in Model D, these strategies produce unrealistically high velocity values near the surface, whereas our method yields more accurate and plausible results. The acquisition pattern learned by our method avoids purely geometric configurations and instead strategically retains sources that maximize subsurface illumination and reconstruction fidelity. These results confirm that our method not only achieves better numerical performance (as shown in Table II) but also offers practical advantages in resolving fine-scale geological features under severe undersampling, making it a robust tool for acquisition design in real-world seismic imaging scenarios.

I. Experiment III: Simultaneous receivers and shots pattern design

This experiment focuses on optimizing receiver and source locations simultaneously. Table III reports quantitative results for velocity models F and G. Among the baselines, the uniform pattern performs well at low acquisition rates (e.g., $\gamma = 0.1$), occasionally surpassing the proposed method due to its regular spatial coverage and reduced aliasing under mild sparsity. This suggests that regular sampling remains effective when sufficient measurements are available. However, as sparsity increases, uniformity degrades significantly, while the proposed method maintains consistently strong performance across all metrics. Qualitative comparisons in Fig. 3 further highlight the robustness of the proposed approach. For instance, in model F, the uniform pattern overestimates layer thickness, whereas the proposed pattern accurately preserves it. In model G, the uniform, jittered, random, and end-to-end patterns introduce velocity artifacts in the upper section that are absent with the proposed strategy. This improvement may result from the optimized pattern avoiding excessive receiver removal near key structural transitions (e.g., between interfaces) and instead concentrating measurements where they maximize subsurface illumination. The proposed sampling strategy is designed to enhance both reconstruction fidelity and target illumination under severe data constraints.

J. Experiment IV: 3D seismic pattern design

This experiment evaluates the performance of the proposed method for 3D seismic acquisitions. This case evaluates the design of the 3D receiver pattern. Figure 4 compares the seismic pattern φ^* optimized by our method with state-of-the-art patterns: random, uniform, and jittered. The optimized pattern tends to remove more receivers when the velocity model has lower structural complexity. For example, in the single-fault model, more traces are removed at the edges since the fault runs through the entire model. The anticline model removes fewer receivers at the center because most of the layers can be illuminated there. The graben model is a symmetric structure; therefore, the optimized pattern tends to remove receivers that are homogeneously distributed across the acquisition area.

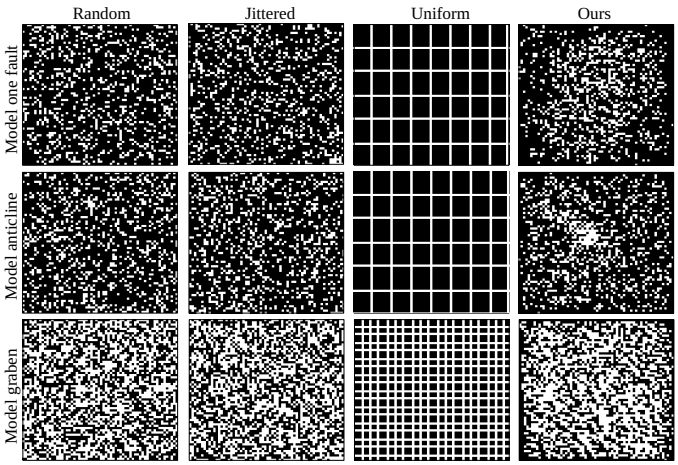

Fig. 4. Seismic pattern design of the three 3D velocity models under study. Single-fault and anticline models have a 20% undersampling rate, and graben models a 50% undersampling rate. Black and white points represent the removed and acquired receivers, respectively.

TABLE III

SIMULTANEOUS RECEIVERS AND SOURCES PATTERN DESIGN. COMPARISON OF AVERAGE QUANTITATIVE METRICS FOR THE VELOCITY MODELS D-E AT DIFFERENT UNDERSAMPLING RATES. MSE AND MAE VALUES ARE IN THE ORDER OF $\times 10^{-2}$. BOLD NUMBERS REPRESENT THE BEST PERFORMANCE METRIC.

%γ	Uniform				Jittered				Random				End-to-end				ISPO (our)			
	LPIPS ↓	MSE ↓	MAE ↓	SSIM ↑	LPIPS ↓	MSE ↓	MAE ↓	SSIM ↑	LPIPS ↓	MSE ↓	MAE ↓	SSIM ↑	LPIPS ↓	MSE ↓	MAE ↓	SSIM ↑	LPIPS ↓	MSE ↓	MAE ↓	SSIM ↑
10	**0.085**	**0.59**	**4.82**	**0.830**	0.120	1.60	6.70	0.791	0.100	1.13	5.87	0.809	0.102	0.81	5.33	0.828	0.100	0.68	5.24	0.814
20	0.182	1.98	9.53	0.698	0.238	9.49	16.13	0.631	0.227	6.84	14.22	0.646	0.278	8.15	18.68	0.538	**0.146**	**1.63**	**7.96**	**0.755**
30	**0.237**	**4.06**	**13.07**	0.629	0.275	13.04	20.09	0.571	0.262	9.88	17.68	0.592	0.328	27.04	30.08	0.464	0.243	5.64	13.77	**0.633**
40	**0.283**	**9.38**	**18.97**	**0.559**	0.311	18.88	25.70	0.494	0.311	18.67	25.99	0.484	0.355	29.12	33.74	0.387	0.329	20.11	27.83	0.458
50	0.301	12.69	23.73	0.466	0.325	20.28	28.39	0.439	0.320	18.21	27.14	0.450	0.449	49.51	49.03	0.253	**0.274**	**9.69**	**20.18**	**0.519**

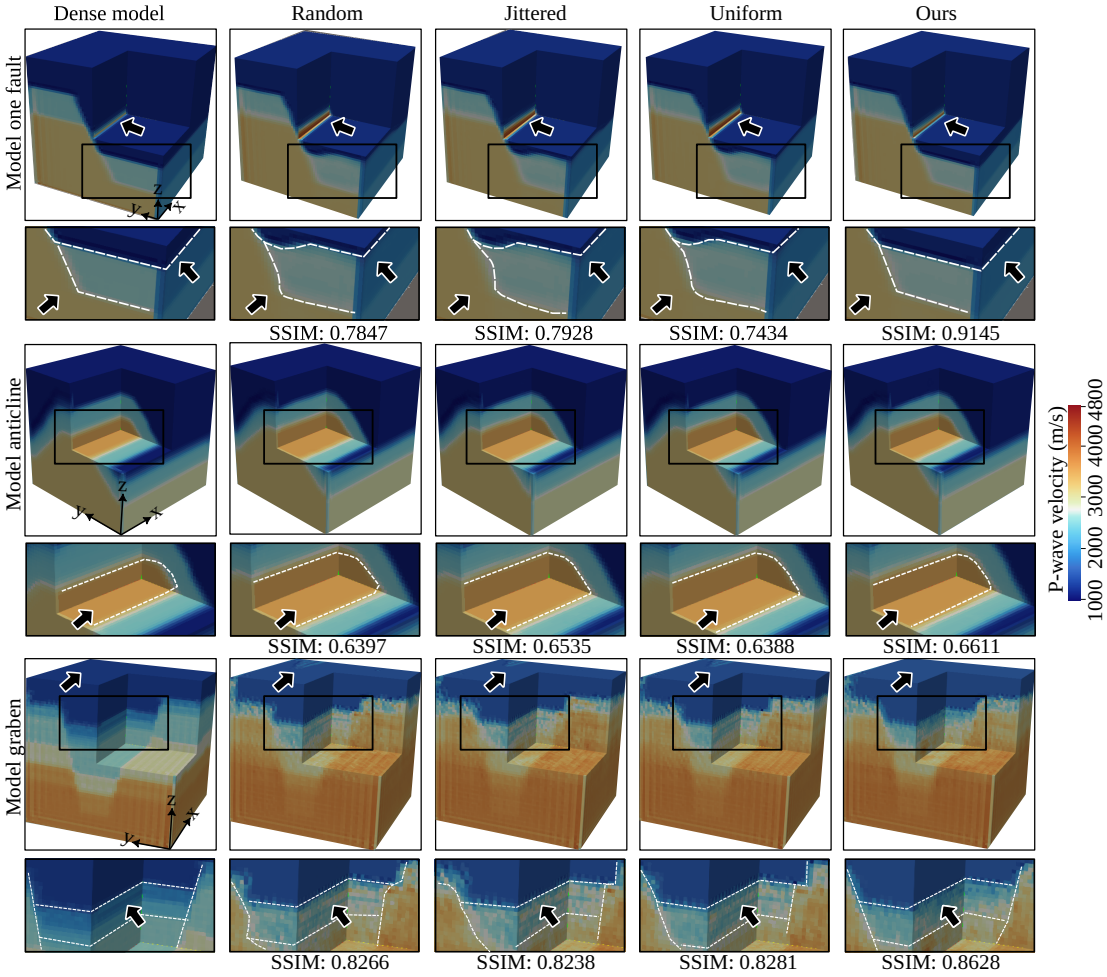

Fig. 5. Comparison between 3D reconstructed velocity models of uniform, random, jittered, and our optimized pattern with $\gamma = 80\%$. White dashed lines represent interfaces to highlight the differences. Black and white points represent the removed and acquired receivers, respectively.

Figure 5 compares the reconstructed velocity models for a 3D case with a single fault under different acquisition patterns: dense, random, jittered, uniform, and the proposed method. Random, jittered, and uniform undersampling strategies fail to accurately preserve the geometry of the cyan layer, which appears artificially thickened and less consistent across the fault. In contrast, the proposed method maintains the true layer thickness and structural continuity, closely resembling the reference model. Quantitative metrics indicate that the optimized pattern outperforms the baseline patterns, achieving an SSIM improvement of 0.1711.

IV. DISCUSSION

State-of-the-art approaches different from baseline patterns include an end-to-end [22] framework, where the optimization of seismic patterns is carried out as follows:

$$\theta^*, \varphi_c^* = \arg\min_{\theta,\varphi_c} \frac{\rho_1}{MNO} \left\| \mathcal{N}_\theta(\mathcal{M}_{\varphi_c}(\mathcal{P})) - \mathcal{P} \right\|_2^2 + \rho_2 \mathcal{L}_c, \qquad c \in \{R, P, B\}. \tag{22}$$

where $\mathcal{N}_\theta$ is a reconstruction neural network with trainable parameters θ with a U-net arquitecture [44]. This method optimizes acquisition patterns based on the quality of shot reconstruction. However, high-fidelity shot reconstruction does

not necessarily guarantee optimal wavefield diversity or subsurface coverage, particularly for complex reflection events that are critical for accurate subsurface imaging. In contrast, the proposed method explicitly guides the pattern optimization using a differentiable imaging operator that enforces consistency in geological structures and velocity values. To ensure that the learned pattern is also effective in signal reconstruction or other constraints, we also propose to compare the proposed method in a reconstruction-based approach as follows:

$$\theta^*, \varphi_c^* = \arg\min_{\theta,\varphi_c} \frac{\rho_1}{MNO} \left\| \mathcal{G}_{\omega^*}(\mathcal{M}_{\varphi_c}(\mathcal{P})) - \mathcal{G}_{\omega^*}(\mathcal{P}) \right\|_2^2 + \frac{\rho_2}{MNO} \left\| \mathcal{N}_\theta(\mathcal{M}_{\varphi_c}(\mathcal{P})) - \mathcal{P} \right\|_2^2 + \rho_3 \mathcal{L}_c, \qquad c \in \{R, P, B\}. \tag{23}$$

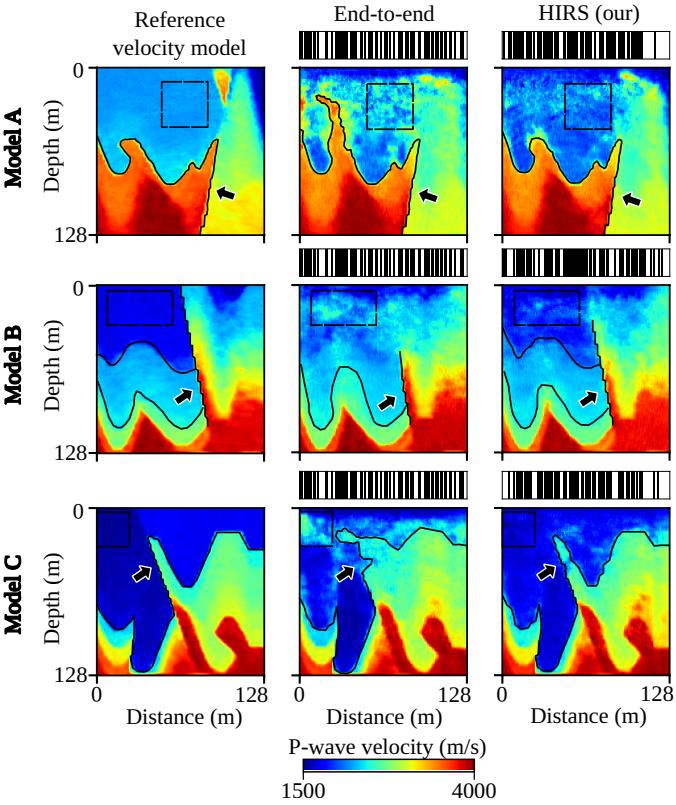

Fig. 6. Comparison of reconstructed velocity models using the end-to-end and end-to-end + Proposed. Black vertical lines represent the removed receivers.

This formulation, henceforth called the hybrid imaging-reconstruction scheme (HIRS), was computed using $\rho_1 = 2^{-0.16E}$, $\rho_2 = 0.05$, and $\rho_3 = 10$, which were selected using the Hyperopt grid search technique delineate lateral variations within the layers resulting velocity models, which use the optimized pattern from Equations 22 and 23 as input. The pattern optimized by end-to-end tends to produce velocity artifacts (black boxes) and fails to delineate lateral variations within the layers accurately. In contrast, HIRS prioritizes acquisition geometries that better capture subsurface complexity, thereby improving velocity model reconstruction under identical acquisition constraints. Table IV reports the quantitative metrics for both velocity and seismic data reconstruction.

HIRS consistently outperforms across different undersampling rates, while the reconstructed data remains competitive with the end-to-end approach. In particular, HIRS achieves lower MSE and MAE values, as well as higher SSIM scores, in velocity model reconstruction, indicating improved accuracy and structural fidelity. Notably, at the most challenging acquire ratio ($\gamma = 0.5$), HIRS reduces the MSE by nearly 66% (from 10.06 to 3.37) and the MAE by over 6 units, while increasing the SSIM from 0.5278 to 0.6184. These improvements demonstrate the method's robustness in preserving spatial continuity and reducing artifacts in the recovered subsurface structures. Although the end-to-end baseline yields slightly better results in reconstructing seismic data, particularly in terms of SSIM and PSNR (e.g., $\gamma = 0.9$), the HIRS method provides a better trade-off by promoting more geologically consistent velocity models. As γ increases, the HIRS method maintains stable performance on seismic data metrics while significantly improving subsurface velocity estimation quality. Overall, the proposed strategy regularizes seismic design by guiding it toward acquisition patterns that not only effectively recover missing traces but also yield superior reconstruction of geologically meaningful velocity models. This highlights its potential for more reliable subsurface illumination and interpretation in seismic imaging tasks.

TABLE IV
AVERAGE QUANTITATIVE METRICS FOR END-TO-END AND HIRS METHODS FOR THE RECONSTRUCTION OF VELOCITY MODELS AND SEISMIC DATA. MSE AND MAE VALUES ARE IN THE ORDER OF $\times 10^{-2}$. BOLD NUMBERS REPRESENT THE BEST PERFORMANCE.

	End-to-end velocity models				End-to-end reconstructed data			
%γ	**LPIPS ↓**	**MSE ↓**	**MAE ↓**	**SSIM ↑**	**MSE ↓**	**SSIM ↑**	**PSNR ↑**	**SNR ↑**
90	**0.048**	0.20	2.85	0.894	0.40	0.967	24.178	13.592
80	0.108	0.63	4.90	0.817	0.40	0.962	24.104	13.518
70	0.178	1.57	7.54	0.733	0.41	0.955	24.002	13.416
60	0.259	4.61	12.08	0.630	0.44	0.937	23.729	13.143
50	0.318	10.06	17.98	0.528	0.45	0.927	23.611	13.025
	HIRS (our) velocity models				HIRS (our) reconstructed data			
90	0.049	**0.19**	**2.82**	**0.895**	0.48	0.933	23.322	12.736
80	**0.094**	**0.45**	**4.28**	**0.832**	0.71	0.762	21.555	10.969
70	**0.159**	**1.04**	**6.32**	**0.758**	1.24	0.736	19.117	8.531
60	**0.211**	**1.70**	**8.19**	**0.700**	1.27	0.586	18.991	8.405
50	**0.259**	**3.37**	**11.40**	**0.618**	0.76	0.850	21.321	10.735

V. PLAUSIBLE SCENARIOS IN WHICH THE APPROACH OF ISPO COULD BE HELPFUL TO

Seismic acquisition geometry design is fundamentally linked to maximizing subsurface illumination while balancing cost, practical constraints, and geological uncertainty. From a geophysical perspective, the proposed ISPO framework is particularly appealing because it integrates imaging constraints, data-driven geological variability, and source–receiver optimization within a unified deep learning (DL) formulation. Below, we discuss several plausible real-world scenarios in which ISPO could provide substantial benefits for seismic exploration and monitoring.

- **Exploration in geologically complex areas with uncertain subsurface structure.** Regions characterized by

strong lateral heterogeneity, faulting, or salt-related deformation pose severe challenges for classical acquisition design. Illumination gaps, shadow zones, and variable reflector geometry require survey designs that can adapt to complex structural patterns. Recent works on target-oriented survey design underscore these challenges and the importance of imaging-based optimization [13]. ISPO is well-suited for such environments because:

1) The diffusion-based perturbation model generates geologically realistic variations around a reference velocity model, allowing the design to be tested against multiple plausible scenarios.
2) Imaging-guided optimization ensures that the resulting pattern maximizes subsurface illumination of structures most affected by lateral variability (faults, folds, intrusions).
3) This is particularly helpful in structurally complex basins (e.g., accretionary wedges, fold-and-thrust belts), where illumination varies rapidly with depth and lateral position.

This makes ISPO a competitive alternative to computationally expensive model-based approaches (e.g., full-wavefield migration–based design [13] or ergodic sampling [16]), especially when only approximate subsurface information is available.

- **Acquisition with severe operational constraints (environmental, social, or logistical).** Field acquisition is increasingly constrained by environmental protection, land access, infrastructure, and community considerations. As a result, irregular or sparse acquisition geometries have become common in modern seismic programs. Traditional uniform designs often cannot be implemented in such contexts. ISPO provides value in these scenarios because:

  1) It can optimize sparse patterns of receivers or sources, maximizing illumination despite missing stations.
  2) The binary layer can encode forbidden zones, making the optimization fully compliant with surface restrictions.
  3) The reconstructed velocity map performance under severe subsampling (e.g., $\gamma = 30\%$–50%) is consistently superior to classical jittered or random sampling approaches (Tables I–III).

  This capability aligns with modern irregular acquisition strategies that aim to reduce costs and environmental impact while preserving imaging quality, as highlighted in recent surveys [15], [16].
- **Frontier exploration with limited prior information**. In frontier areas—deepwater margins, remote onshore basins, or regions with limited well control—prior velocity models are often crude or incomplete. The ability to incorporate uncertainty into survey design is therefore essential. ISPO contributes by:
  - Generating perturbed models through diffusion sampling that represent plausible geological configurations consistent with the available prior.
  - Optimizing patterns that remain robust to variations between the reference and actual subsurface—an ability identified as highly desirable in DL-based acquisition design [22].
  - Reducing the risk of program failure associated with under-illumination of critical targets by testing the pattern against multiple synthetic subsurface scenarios.

  This robustness is essential when conducting reconnaissance seismic campaigns to delineate basin structure or map early leads.
- **Seismic imaging of shallow anomalies and near-surface complexity.** Shallow gas pockets, complex weathered layers, or low-velocity anomalies significantly degrade seismic illumination. Several recent studies show that acquisition geometry strongly affects near-surface recovery and target imaging performance [12], [14]. ISPO can help because:
  - The imaging-guided constraint encourages source–receiver arrangements that improve illumination of shallow anomalies.
  - The framework does not strictly depend on uniform sampling and can adapt receiver density to shallow-layer heterogeneity.
  - Perturbation-based optimization trains the pattern across realistic shallow-layer variability, improving robustness to uncertainties in the weathered zone.

  This scenario is critical for land exploration, shallow hazard mapping, and offshore engineering surveys.
- **Advantages and limitations of the imaging operator:** A key advantage of training $\mathcal{G}_\omega$ on diffusion-perturbed velocity models is that the optimized acquisition pattern becomes robust to plausible model uncertainty, improving structural consistency under aggressive undersampling. In particular, this strategy stabilizes the optimization objective and reduces sensitivity to a single deterministic reference model. A limitation is that the learned operator inherits the support of the training distribution and therefore may not generalize to geological configurations far outside the reference regime. Extending generalization across multiple geological families can be achieved by incorporating multi-prior ensembles or broader generative priors, although this is not the main objective of ISPO, which targets survey design within a known exploration setting.

  Relevance of target or reference model to exploration practice: Survey design is commonly performed using incomplete prior information, while final high-resolution inversion is carried out only after acquisition. ISPO fits naturally within this workflow: it provides a principled way to optimize acquisition under uncertainty given a best-available prior, while remaining compatible with downstream physics-based inversion methods (e.g., FWI or least-squares migration) once field data become available.

VI. Conclusions

We presented ISPO (Imaging-guided Seismic Pattern Optimization), a novel deep learning-based framework for seismic acquisition design that directly incorporates imaging fidelity into the optimization of source and receiver geometries. Unlike state-of-the-art methods that rely solely on signal reconstruction or heuristic design patterns, ISPO introduces an imaging constraint and employs conditional diffusion models to simulate realistic geological perturbations. Through extensive experiments, ISPO demonstrated superior performance in reconstructing velocity models and preserving geological structures, even at extremely high data sparsity. These results confirm that integrating imaging-guided priors into the acquisition design process enables more resilient, accurate, and efficient subsurface characterization. ISPO provides a scalable and adaptable tool for next-generation seismic survey planning in complex geophysical conditions. Furthermore, the incorporation of data-driven frameworks, such as the proposed HIRS method, enables the integration of ISPO across different tasks for seismic pattern design.

Academic dissemination

International Conferences

1) **A. Mantilla-Dulcey** and H. Arguello. Deep Learning-Based Seismic Acquisition Pattern Design Guided by Velocity Model Imaging. 2025 XXV Symposium of Image, Signal Processing, and Artificial Vision (STSIVA), Armenia, Colombia, 2025, pp. 1-5, doi: 10.1109/STSIVA66383.2025.11156396.
2) **A. Mantilla-Dulcey.,** J. Torres-Quintero and H. Arguello. 3D Seismic Acquisition Design Optimization Regularized by FWI: A Deep Learning Approach. 2025 IEEE International Workshop on Computational Advances in Multi-Sensor Adaptive Processing (CAMSAP), Punta Cana, República Dominicana, 2025.
3) L. Suarez-Rodriguez, R. Jacome, R. Gualdron-Hurtado, **A. Mantilla-Dulcey** and H. Arguello. DICE: Diffusion Consensus Equilibrium for Sparse-view CT Reconstruction. 2025 IEEE International Workshop on Computational Advances in Multi-Sensor Adaptive Processing (CAMSAP), Punta Cana, República Dominicana, 2025.

National Conferences

1) **A. Mantilla-Dulcey**, L. Suarez-Rodriguez, L. Rodriguez, J. Torres-Quintero, P. Goyes, H. Arguello. Nuevas tecnologías computacionales para el procesamiento e inversión conjunta de gravimetría, magnetometría y magnetotelúrica mediante aprendizaje profundo guiado por principios físicos para la caracterización multicriterio. XX Congreso Colombiano de Geología, Cali, Colombia, 2025.

Academic papers

1) **A. Mantilla-Dulcey** and H. Arguello (2025). Imaging guided pattern optimization for seismic acquisition geometries design with deep learning. Submitted to IEEE Transactions on Geoscience and Remote Sensing.
2) J. Torres-Quintero, P. Goyes-Peñafiel, **A. Mantilla-Dulcey**, L. Rodríguez-López, J. Sanabria-Gómez, and H. Arguello (2025). Poststack seismic data denoising via dynamic guided learning. The Leading Edge, 44(9), 692-704.

Grants

1) **A. Mantilla-Dulcey**, A. Alvarez-Naranjo and H. Arguello (2025). Plataforma inteligente de monitoreo y gestión del riesgo de la susceptibilidad a incendios forestales de la cobertura vegetal integrando tecnologías geoespaciales e inteligencia artificial para la generación de alertas tempranas en Colombia. Convocatoria Orquídeas: Mujeres en Inteligencia Artificial, Ciencias y Tecnologías Cuánticas 2025.

Honors

1) **A. Mantilla-Dulcey**, L.M Rodríguez, L. Suárez, and H. Arguello (2024). FIRENET. Segundo puesto a nivel nacional del concurso Datos a la U de MinTIC.

Research Projects

1) Proyecto 3925. Modelamiento matemático-computacional para el mejoramiento de imágenes sísmicas en cuencas emergentes colombianas utilizando adaptación de dominio. Institución financiadora: Universidad Industrial de Santander. Participación: Profesional.
2) Proyecto CTO 045-2025. Nuevas tecnologías computacionales para el procesamiento e inversión conjunta de gravimetría, magnetometría y magnetotelúrica mediante aprendizaje profundo guiado por principios físicos para la caracterización multicriterio. Institución financiadora: Ministerio de Ciencia, Tecnología e Innovación (MINCIENCIAS) y Agencia Nacional de Hidrocarburos. Participación: Estudiante de maestría.

References

[1] A. Pommeret, F. Ricci, and K. Schubert, "Critical raw materials for the energy transition," *European Economic Review*, vol. 141, p. 103991, 2022. [Online]. Available: https://www.sciencedirect.com/science/article/pii/S0014292121002683

[2] M. Zhang and Y. Li, "The role of geophysics in geologic hydrogen resources," *Journal of Geophysics and Engineering*, p. gxae056, 2024.

[3] A. Asrillah, A. Abdullah, K. Bauer, B. Norden, and C. M. Krawczyk, "Fracture characterisation using 3-d seismic reflection data for advanced deep geothermal exploration in the ne german basin," *Geothermics*, vol. 116, p. 102833, 2024.

[4] N. J. Gardiner, J. J. Roberts, G. Johnson, D. J. Smith, C. E. Bond, R. Knipe, S. Haszeldine, S. Gordon, and M. O'Donnell, "Geosciences and the energy transition," *Earth Science, Systems and Society*, vol. 3, no. 1, p. 10072, 2023.

[5] C. Wu, R. Xu, L. Han, B. Feng, and H. Wang, "Optimal stack with illumination-based weighting," *IEEE Transactions on Geoscience and Remote Sensing*, vol. 63, pp. 1–12, 2025.

[6] R. Singh, A. Srivastava, R. Kant, S. Maurya, P. Mahadasu, N. Verma, G. Hema, P. Kushwaha, Richa, K. Singh *et al.*, "Integrated thin layer classification and reservoir characterization using sparse layer reflectivity inversion and radial basis function neural network: a case study," *Marine Geophysical Research*, vol. 45, no. 1, p. 3, 2024.

[7] B. Qiao, Y. Lu, Q. Li, Y. Huang, and S. Liang, "Data-driven reflection imaging based on seismic interferometry," *Geophysics*, vol. 87, no. 4, pp. Q15–Q29, 2022.

[8] X. Wu, L. Liang, Y. Shi, and S. Fomel, "Faultseg3d: Using synthetic data sets to train an end-to-end convolutional neural network for 3d seismic fault segmentation," *Geophysics*, vol. 84, no. 3, pp. IM35–IM45, 2019.

[9] W. Zhang and J. Gao, "Deep-learning full-waveform inversion using seismic migration images," *IEEE Transactions on Geoscience and Remote Sensing*, vol. 60, pp. 1–18, 2021.

[10] D. A. Herron, *First steps in seismic interpretation*. Society of Exploration Geophysicists, 2011.

[11] J. Blanch, J. Jarvis, C. Hurren, A. Kostin, Y. Liu, and L. Hu, "Designing an exploration-scale obn: Acquisition design for subsalt imaging and velocity determination," *The Leading Edge*, vol. 39, no. 4, pp. 248–253, 2020.

[12] S. Coskun, R. R. Stewart, E. Baysal, and A. Aydemir, "Optimum designs for 2-d and 3-d seismic surveys via modeling and reverse-time migration: Pierce junction salt dome, texas," *Surveys in Geophysics*, pp. 1–26, 2021.

[13] B. Revelo-Obando and G. Blacquière, "Target-oriented acquisition geometry design based on full-wavefield migration," *Geophysics*, vol. 89, no. 3, pp. P21–P32, 2024.

[14] A. H. A. Latiff, D. P. Ghosh, and N. M. A. Latiff, "Optimizing acquisition geometry in shallow gas cloud using particle swarm optimization approach," *International Journal of Computational Intelligence Systems*, vol. 10, no. 1, pp. 1198–1210, 2017.

[15] S. Wu, D. J. Verschuur, and G. Blacquière, "Automated seismic acquisition geometry design for optimized illumination at the target: A linearized approach," *IEEE Transactions on Geoscience and Remote Sensing*, vol. 60, pp. 1–13, 2021.

[16] M. Zhang and Y. Li, "Ergodic sampling: Acquisition design to maximize information from limited samples," *Geophysical Prospecting*, vol. 72, no. 2, pp. 435–467, 2024.

[17] V. Winner, P. Edme, and H. Maurer, "Model-based optimization of source locations for 3d acoustic seismic full-waveform inversion," *Geophysical Prospecting*, vol. 71, no. 1, pp. 3–16, 2022.

[18] M. Nagendra Babu, B. Baskey, V. G. Thota, and S. Singh, "Evaluation of 3d seismic survey design parameters through ray-trace modeling and seismic illumination studies: a case study," *Journal of Petroleum Exploration and Production Technology*, vol. 12, no. 11, pp. 3021–3031, 2022.

[19] M. Zhang, "Compressive sensing acquisition with application to marchenko imaging," *Pure and Applied Geophysics*, vol. 179, no. 6, pp. 2383–2404, 2022.

[20] A. Curtis, "Theory of model-based geophysical survey and experimental design: part 1—linear problems," *The Leading Edge*, vol. 23, no. 10, pp. 997–1004, 2004.

[21] A. Titova, M. B. Wakin, and A. C. Tura, "Achieving robust compressive sensing seismic acquisition with a two-step sampling approach," *Sensors*, vol. 23, no. 23, p. 9519, 2023.

[22] A. Hernandez-Rojas and H. Arguello, "Design of undersampled seismic acquisition geometries via end-to-end optimization," *IEEE Transactions on Geoscience and Remote Sensing*, 2023.

[23] P. Goyes-Peñafiel, L. Suárez-Rodríguez, C. V. Correa, and H. Arguello, "Gan–supervised seismic data reconstruction: An enhanced–learning for improved generalization," *IEEE Transactions on Geoscience and Remote Sensing*, 2024.

[24] G. Blacquière and S. Nakayama, "Optimum seismic acquisition geometry design with the help of artificial intelligence," in *SEG International Exposition and Annual Meeting*. SEG, 2019, p. D043S094R006.

[25] X. Wang, Z. Wang, X. Lei, C. Zhu, and J. Gao, "Seis-pddn: Seismic undersampling design and reconstruction using prior distribution and diffusion null-space iteration," *IEEE Transactions on Geoscience and Remote Sensing*, 2024.

[26] J. Ho, A. Jain, and P. Abbeel, "Denoising diffusion probabilistic models," *Advances in neural information processing systems*, vol. 33, pp. 6840–6851, 2020.

[27] P. Goyes-Peñafiel, U. S. Kamilov, and H. Arguello, "Cddip: Constrained diffusion-driven deep image prior for seismic data reconstruction," *IEEE Geoscience and Remote Sensing Letters*, 2025.

[28] N. Ricker, "Further developments in the wavelet theory of seismogram structure," *Bulletin of the Seismological Society of America*, vol. 33, no. 3, pp. 197–228, 1943.

[29] M. Courbariaux, I. Hubara, D. Soudry, R. El-Yaniv, and Y. Bengio, "Binarized neural networks: Training deep neural networks with weights and activations constrained to+ 1 or-1," *arXiv preprint arXiv:1602.02830*, 2016.

[30] Y. Bengio, N. Léonard, and A. Courville, "Estimating or propagating gradients through stochastic neurons for conditional computation," *arXiv preprint arXiv:1308.3432*, 2013.

[31] C. Deng, S. Feng, H. Wang, X. Zhang, P. Jin, Y. Feng, Q. Zeng, Y. Chen, and Y. Lin, "Openfwi: Large-scale multi-structural benchmark datasets for full waveform inversion," *Advances in Neural Information Processing Systems*, vol. 35, pp. 6007–6020, 2022.

[32] M. De la Varga, A. Schaaf, and F. Wellmann, "Gempy 1.0: open-source stochastic geological modeling and inversion," *Geoscientific Model Development*, vol. 12, no. 1, pp. 1–32, 2019.

[33] Center for Subsurface Imaging and Fluid Modeling (CSIM), "Seismic inversion - finite difference lab," n.d., accessed: 2024. [Online]. Available: https://csim.kaust.edu.sa/files/SeismicInversion/Chapter.FD/lab.FD2.8/lab.html

[34] R. Zhang, P. Isola, A. A. Efros, E. Shechtman, and O. Wang, "The unreasonable effectiveness of deep features as a perceptual metric," in *Proceedings of the IEEE conference on computer vision and pattern recognition*, 2018, pp. 586–595.

[35] C. Lu, Y. Wang, X. Zou, J. Zong, and Q. Su, "Elastic full-waveform inversion via physics-informed recurrent neural network," *IEEE Transactions on Geoscience and Remote Sensing*, 2024.

[36] Y. Lin, J. Theiler, and B. Wohlberg, "Physics-guided data-driven seismic inversion: Recent progress and future opportunities in full-waveform inversion," *IEEE Signal Processing Magazine*, vol. 40, no. 1, pp. 115–133, 2023.

[37] Y. Wu and Y. Lin, "Inversionnet: An efficient and accurate data-driven full waveform inversion," *IEEE Transactions on Computational Imaging*, vol. 6, pp. 419–433, 2019.

[38] M. Araya-Polo, J. Jennings, A. Adler, and T. Dahlke, "Deep-learning tomography," *The Leading Edge*, vol. 37, no. 1, pp. 58–66, 2018.

[39] W. Wang, F. Yang, and J. Ma, "Velocity model building with a modified fully convolutional network," in *SEG International Exposition and Annual Meeting*. SEG, 2018, pp. SEG–2018.

[40] B. Liu, S. Yang, Y. Ren, X. Xu, P. Jiang, and Y. Chen, "Deep-learning seismic full-waveform inversion for realistic structural models," *Geophysics*, vol. 86, no. 1, pp. R31–R44, 2021.

[41] A. Alali, V. Kazei, M. Kalita, and T. Alkhalifah, "Deep learning unflooding for robust subsalt waveform inversion," *Geophysical Prospecting*, vol. 72, no. 1 Machine learning applications in geophysical exploration and monitoring, pp. 7–19, 2023.

[42] Y. Li and T. Alkhalifah, "Target-oriented time-lapse elastic full-waveform inversion constrained by deep learning-based prior model," *IEEE Transactions on Geoscience and Remote Sensing*, vol. 60, pp. 1–12, 2022.

[43] O. Oktay, J. Schlemper, L. L. Folgoc, M. Lee, M. Heinrich, K. Misawa, K. Mori, S. McDonagh, N. Y. Hammerla, B. Kainz *et al.*, "Attention u-net: Learning where to look for the pancreas," *arXiv preprint arXiv:1804.03999*, 2018.

[44] O. Ronneberger, P. Fischer, and T. Brox, "U-net: Convolutional networks for biomedical image segmentation," in *Medical image computing and computer-assisted intervention–MICCAI 2015: 18th international conference, Munich, Germany, October 5-9, 2015, proceedings, part III 18*. Springer, 2015, pp. 234–241.

[45] J. Bacca, T. Gelvez-Barrera, and H. Arguello, "Deep coded aperture design: An end-to-end approach for computational imaging tasks," *IEEE Transactions on Computational Imaging*, vol. 7, pp. 1148–1160, 2021.

[46] R. Jacome, P. Gomez, and H. Arguello, "Middle output regularized end-to-end optimization for computational imaging," *Optica*, vol. 10, no. 11, pp. 1421–1431, 2023.

[47] M. Marquez, Y. Lai, X. Liu, C. Jiang, S. Zhang, H. Arguello, and J. Liang, "Deep-learning supervised snapshot compressive imaging enabled by an end-to-end adaptive neural network," *IEEE Journal of Selected Topics in Signal Processing*, vol. 16, no. 4, pp. 688–699, 2022.

[48] R. Jacome, J. Bacca, and H. Arguello, "Deep-fusion: An end-to-end approach for compressive spectral image fusion," in *2021 IEEE International Conference on Image Processing (ICIP)*. IEEE, 2021, pp. 2903–2907.

[49] A. Alblwi, S. Makkawy, and K. E. Barner, "D-ddpm: Deep denoising diffusion probabilistic models for lesion segmentation and data generation in ultrasound imaging," *IEEE Access*, 2025.

[50] H. Jiang, M. Imran, T. Zhang, Y. Zhou, M. Liang, K. Gong, and W. Shao, "Fast-ddpm: Fast denoising diffusion probabilistic models for medical image-to-image generation," *IEEE Journal of Biomedical and Health Informatics*, 2025.

[51] D. Qosja, S. Wagner, and D. O'Hagan, "Sar image synthesis with diffusion models," in *2024 IEEE Radar Conference (RadarConf24)*. IEEE, 2024, pp. 1–6.